JCTC Journal of Chemical Theory and Computation

Article

pubs.acs.org/JCTC

Amyloid β Fibril Elongation by Monomers Involves Disorder at the Tip

Marco Bacci, Jiří Vymětal,[†] Maja Mihajlovic,[‡] Amedeo Caflisch,* and Andreas Vitalis*

University of Zurich, Department of Biochemistry, Winterthurerstrasse 190, CH-8057 Zurich, Switzerland

Web-Enhanced Feature Supporting Information

ABSTRACT: The growth of amyloid fibrils from $A\beta_{1-42}$ peptide, one of the key pathogenic players in Alzheimer's disease, is believed to follow a nucleation−elongation mechanism. Fibril elongation is often described as a "dock−lock" procedure, where a disordered monomer adsorbs to an existing fibril in a relatively fast process (docking), followed by a slower conformational transition toward the ordered state of the template (locking). Here, we use molecular dynamics simulations of an ordered pentamer of Aβ42 at fully atomistic resolution, which includes solvent, to characterize the elongation process. We construct a Markov state model from an ensemble of short trajectories generated by an advanced sampling algorithm that efficiently diversifies a subset of the system without any bias forces. This subset corresponds to selected dihedral angles of the peptide chain at the fibril tip favored to be the fast growing one experimentally. From the network model, we extract distinct locking pathways covering time scales in the high microsecond regime. Slow steps are associated with the exchange of hydrophobic contacts, between nonnative and native intermolecular contacts as well as between intra- and intermolecular ones. The N-terminal segments, which are disordered in fibrils and typically considered inert, are able to shield the lateral interfaces of the pentamer. We conclude by discussing our findings in the context of a refined dock−lock model of Aβ fibril elongation, which involves structural disorder for more than one monomer at the growing tip.

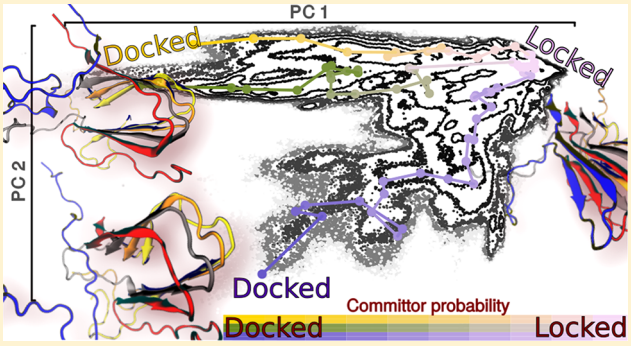

INTRODUCTION

The aggregation of proteins and peptides is associated with a number of human diseases, including Alzheimer's (AD) and Parkinson's.[1] AD symptoms are both cognitive and behavioral in nature and involve the well-known progressive deficiencies in memory, speech, and decision making but also include depression, irritability, and agitation.[2] At the neurophysiological level, cerebral atrophy including loss of neurons occurs and aggregates rich in amyloid β peptide (extracellular plaques) or hyperphosphorylated tau (neurofibrillary tangles forming intracellularly) appear, yet the connections between these processes have not been fully elucidated.[3] The amyloid β peptide is known to aggregate *in vitro* into fibrils, which share some but not all structural properties with *in vivo* plaques.[4] In recent years, it has become clear that Aβ can be produced at multiple sites in the cell,[5] is importable, and also aggregates intracellularly.[6,7] These results have provided a rationale for revisions of the amyloid cascade hypothesis[8−10] to account for evidence that extracellular plaques *per se* are less neurotoxic than smaller oligomers[11] or that they are even absent in early AD-afflicted individuals.[12] The dominant forms of Aβ are 40 and 42 residues long, with the latter overrepresented (relative to total concentrations) in plaques,[13] exhibiting faster aggregation, and promoting disease.[14] Fibril formation of these peptides in solution can be described kinetically by a nucleation−elongation scheme.[15,16] *In vitro*, both soluble and precipitated fibrils are polymorphic.[17−19] The term protofibril is defined somewhat loosely, and we will refer to a linear, soluble, and largely ordered assembly with a single molecule per axial unit as a protofibril.

The elongation of soluble Aβ fibrils is a disorder-to-order transition. The monomer, which exists disordered in solution,[20] is thought to dock reversibly to an existing aggregate. A docked monomer can undergo a slow conformational transition, the so-called locking step(s), in which it adopts the structure of the template (see Figure 1A).[21,22] Surface-based single fibril imaging has revealed that elongation occurs in a discrete manner, i.e., productive growth is stepwise and consists of alternating growth and arrest phases.[23−26] Furthermore, elongation has a preferred direction and is about an order of magnitude more rapid at the fast growing end.[26] The arrest phases are thought to correspond to trapped or blocked states of the fibrils, but how this would manifest itself structurally is not clear.[24] Importantly, the step sizes for growth are much larger than the addition of just one monomer even though the adding species is thought to almost exclusively be the monomer.[27] The single fibril traces also reveal that an arrested

Received: June 23, 2017
Published: September 4, 2017

DOI: 10.1021/acs.jctc.7b00662
J. Chem. Theory Comput. 2017, 13, 5117−5130

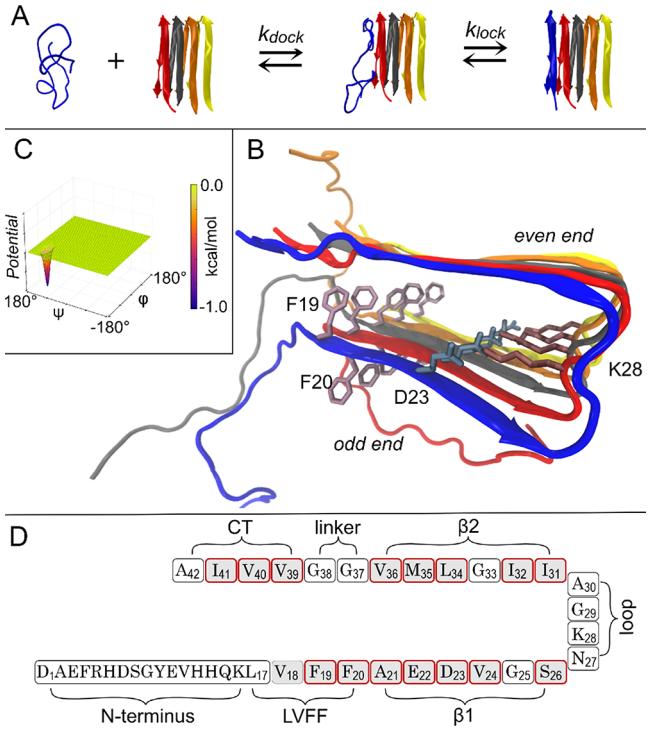

Figure 1. Overview of the process and system under study. (A) Schematic of a monomeric dock–lock mechanism with a single locking step and rigid template. The added monomer is in blue. (B) 3D image[28] of the reconstructed fibrillar pentamer based on the NMR structure. Important residues and interactions are highlighted. Coloring is by chain, and the code is used throughout (chain A is in blue). (C) Representative example of Gaussian well potentials used to stabilize the ϕ/ψ values of the fibrillar states for the residues in chains B–E highlighted by gray boxes in panel D (see Supporting Information, S1.2.1). (D) Schematic and sequence of the Aβ42 monomer. Those residues of chain A in boxes with red outlines were part of the initial PIGS representation. Conversely, the gray background of boxes indicates the application of well potentials for chains B–E.

state does not undergo disassembly to become unblocked and that arrest *per se* has no clear influence on fibril morphology.[23,26] It is difficult to further dissect this "dock–lock" process mechanistically using experiment.

As complementary tools, computer simulations face other issues than experiments. While the structural resolution is limited only by the chosen model, it is no longer clear whether (a) the model depicts reality faithfully or (b) it is possible to observe the model on a sufficiently long time scale. To avoid problem (b), many computational studies on protein aggregation use coarse-grained models. These have provided insight into possible origins of the kinetics of nucleation and elongation including the role of off- and on-pathway disordered oligomers.[29−31] Results from models of this type are limited in that they miss the necessary detail to be clearly identified with specific systems relevant to disease such as Aβ. Furthermore, the high sensitivity of Aβ aggregation to solution conditions such as pH, metal ions, lipids, etc. has been characterized extensively,[32] and this sensitivity suggests that important aspects of the process will never be representable in overly simplified models.

Classical models at full atomistic resolution allow an unequivocal identification of the peptide(s) along with a meaningful representation of solution conditions (whether implicit, explicit, or mixed). Studies of the monomer[33,34] or small oligomers[35−37] in these models highlight disorder along with the resulting sampling problems and an inherent disposition toward β-secondary structure, in particular as oligomers grow. Interestingly, there is not much evidence for extensive regular β-sheet structure in small oligomers observed experimentally,[38,39] although cross-linking enhances β-content with increasing oligomer size.[40] Earlier studies on the elongation problem were limited by sampling problems[41] and/or had to go to artificial conditions to speed up the process,[42] yet in general a picture of a two- or multistep process emerged that seems compatible with experimental evidence.

Recent computational work[43−46] suffers from three common limitations: the presence of a rigidified template, the truncation of the N-termini, and the use of bias forces along a reaction coordinate. A highly ordered template obtained from an ideal starting structure and with restraints/constraints is difficult to reconcile with experiment. While there is strong support for monomers being the primary vehicle of growth, it is known that soluble oligomers[38,39] and even very large assemblies[47,48] can be significantly deficient in terms of both local and long-range order. This means that Aβ monomers must have the ability to dock to many different forms of aggregated Aβ and that these processes contribute to measured rates. In fact, the aforementioned stepwise nature of the growth[23] has suggested a mechanism in which the fibril tip is temporarily blocked, for example by the formation of an elongation-incompetent and kinetically trapped conformation of terminal monomers.[24,25] Importantly, this need not be in conflict with the simple dock–lock scheme (Figure 1A) in kinetic terms as was shown analogously for nucleation.[49] The choice to truncate N-termini is supported by almost all determined structures but contradicted by several mutations in the N-terminal region known to alter the aggregation behavior of Aβ considerably, including a specific impact on elongation.[50,51] In other cases, factors such as production rate can be in play as well.[52] Lastly, the use of bias forces may limit observable pathways. This is because the relaxation behavior in simulations with reaction coordinate biases is known to be difficult to control for "orthogonal" degrees of freedom.[53] For example, if the distance of the centers of mass of two chains is the reaction coordinate, rearrangements that do not change this coordinate are not sped up. Moreover, pathways involving recurrent excursions in this coordinate may even be quenched by the biasing force.

In the present study, we aim to expand on the results in the literature by allowing the elongation process to follow more realistic pathways. For this, we couple a recent advanced sampling method[54] to a complete (all 42 residues) and fully atomistic model of a fibrillar pentamer in a 150 mM aqueous solution of NaCl. Soft, well-type bias potentials are used to gently stabilize the assembly in all but one peptide chain. We obtain an ensemble of continuous trajectories of variable length that is used to construct a network model, which we proceed to analyze in detail. There is no reaction coordinate and no bias force controlling the distance of the target monomer from the assembly in our simulations. This means that the system evolves according to spontaneous fluctuations. Our study will thus be able to complement and extend prior computational work. Han and Schulten[44] in particular employed the same fibril model, although they, as mentioned, neglected the N-termini and rigidified the ordered template. Through a combination of umbrella sampling,[55] hydrogen and solvent coarse-graining,[56] and network and transition path analyses,[57]

DOI: 10.1021/acs.jctc.7b00662
J. Chem. Theory Comput. 2017, 13, 5117−5130

Han and Schulten obtained quantitative predictions regarding the dominant pathways of the elongation of Aβ42 fibrils. These data will be excellent reference points to compare our results to, and we are particularly interested in assessing the influence of the three aforementioned assumptions.

The remainder of the text is structured as follows. Methods are presented as a salient overview (details are given as Supporting Information, specifically sections S1.1−S1.3). We proceed to describe results on the conformational envelope we sampled, network construction, and rates and properties of different locking pathways. We conclude by discussing our findings with regards to the mechanism of elongation, in particular focusing on disorder, growth asymmetry, and the role of the N-termini.

METHODS

System Setup (see Supporting Information, S1.1). Briefly, we extracted a pentameric fibrillar assembly for Aβ17−42 from the first model in the NMR bundle of Lührs et al. (PDB: 2BEG).[58] The missing N-terminal residues were reconstructed and randomized using a Monte Carlo scheme. The system was solvated in a cubic box of 113.7 Å ($\sim 1.5 \times 10^5$ atoms) containing ∼150 mM NaCl in modified Tip3p water. This is the recommended water model for the protein force field we picked, viz., CHARMM36.[59] The system size was large enough to avoid image interactions of peptides irrespective of the tumbling of the assembly. Integration of Newton's equations of motion was used to propagate the system (2 fs time step, constraints on all bonds) in the NVT ensemble at 310 K with two software packages (CAMPARI v3b (http://campari.sourceforge.net) for the enhanced sampling runs and GROMACS 4.6[60] otherwise). The peptide assembly is shown in Figure 1B. It has two ends termed "odd" and "even". We refer to chains as A−E with chain A at the odd end. Chains B−E are subject to well-type potentials (Figure 1C) acting on the ϕ/ψ angles of the residues highlighted in Figure 1D. They were added in anticipation of a decreased structural stability due to the finite size of the system. These potentials stabilize the backbone dihedral angles by at most 1 kcal/mol when in their native values in the β-basin. There is no restoring force acting if the dihedral angles are far away from the native state. There is never any restoring force acting on intermolecular degrees of freedom or on absolute coordinates, and many non-native assemblies are equally compatible with the potential minima.

Simulations (See Supporting Information, S1.2). Since the expected time scale of relevant transitions is extremely slow (up to seconds), simple molecular dynamics (MD) simulations cannot be expected to provide meaningful insight when single trajectories are constrained to the high nanosecond to low microsecond range. We therefore employed an advanced sampling technique called progress index-guided sampling or PIGS[54] that works as follows. Several copies (here, 32) of the same system are evolved under the same conditions. Trajectories diverge because of (required) stochasticity in the propagator (e.g., from the thermostat).[61] Periodically, some trajectories are terminated and reseeded with other putatively more interesting ones. To do this, a state-of-the-art data mining algorithm[62] arranges the data obtained since the last reseeding point and determines which copies are occupying the same area of phase space in a chosen representation. Those copies are deemed redundant and are more likely to be reseeded with copies deemed interesting. The heuristic for interesting rewards replicas that are unique and reside in regions of low sampling density. PIGS has been shown to be an excellent technique for structural diversification when starting from an ordered reference state, in particular if barriers are entropic in nature.[54]

To study elongation at the odd end, we chose to represent the system's essential phase space by the ψ angles of a subset of residues of chain A. This means that the PIGS reseeding decision will aim to diversify this dihedral angle space but have no direct knowledge of the remainder of the assembly. This ability to focus exploration is one of the strengths of the method. We obtained cumulative sampling times of ∼6.2 μs of PIGS simulations with small variations to the subset of dihedral angles and 3.8 μs of canonical MD simulations starting from two native and two nonnative conformations (D1 and D2 below). The complete inventory is found as Tables S1 and S2 (S1.2.2). The two native conformations were considered because of concerns with fibril−internal water molecules and long-lived salt bridges.

Analysis (See Supporting Information, S1.3). Short descriptions of the analysis methodologies are embedded in Results below. A detailed documentation of the entire workflow is given in section S1.3.

RESULTS

Overview of Data Set. We performed a large number of simulations of a pentameric assembly (chains A−E, Figure 1B) of Aβ42 at fully atomistic resolution with a cumulative simulation time of ∼10 μs. The two initial ordered conformations of the system (see section S1.1) were built from the solution NMR structure (2BEG)[58] but with reduced methionine M35. This very model has been demonstrated to be comparatively stable in simulations, including by Han and Schulten.[44] 2BEG is a solution structure of a protofibril, which simplifies the interpretation of elongation by monomer addition relative to a 2- or 3-fold structure. Our choice can thus be regarded as a model system for growth in solution with direct experimental support.

In the simulations, we used well-type potentials to stabilize the intramolecular arrangements of chains B−E in the fibrillar state (Figure 1C,D and section S1.2.1). All simulations evolved the system according to this Hamiltonian, i.e., there was no biasing force acting on a reaction coordinate of binding/unbinding. Using the PIGS advanced sampling method[54] described briefly in Methods, we achieved a focused diversification of a dihedral angle space composed of ψ angles of a subset of residues of chain A (Figure 1D). The initial set comprises all nonglycine residues involved in β-sheets with chain B. Intramolecular conformational changes are a necessary signature of an order-to-disorder transition, and it is thus reasonable to expect them to result in the unlocking of chain A. Since additional details of how the ensemble of trajectories was generated are not essential to what follows, they are presented in Tables S1 and S2 and section S1.2.2.

The total data set comprises $\sim 5 \times 10^6$ snapshots. We first want to understand the envelope of the conformational space sampled by chain A. We consider the six segments outlined in Figure 1D (LVFF, β1, loop, β2, linker, and CT). As Figure 2 shows, the detachment of individual segments is complete when measured by mean in-registry distances. As illustrated by the insets, this does not correspond to a complete unbinding of chain A, which is a limitation. The diversity of docked and unlocked conformations we obtained questions whether a single reaction coordinate such as the center-of-mass distance of A and B (COM-d)[44] can resolve these different structures.

DOI: 10.1021/acs.jctc.7b00662
J. Chem. Theory Comput. 2017, 13, 5117−5130

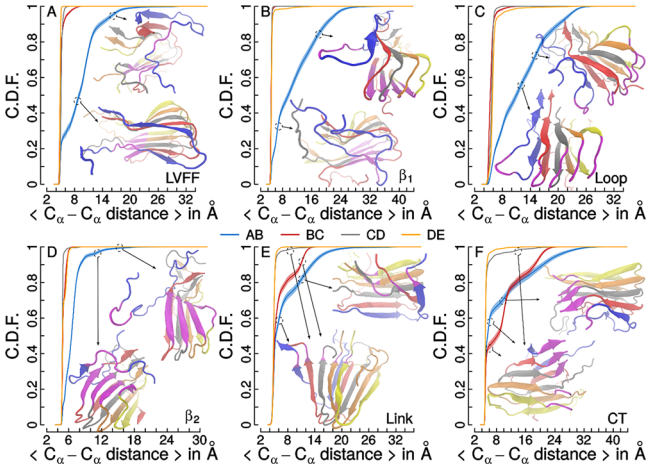

Figure 2. Cumulative distribution functions for mean segment-to-segment distances. Average segment-to-segment distances for all interfaces (color legend in the middle) were computed, and their cumulative distributions across the entire data set are plotted in panels A–F for LVFF, β1, loop, β2, linker, and CT, respectively (see Figure 1D). Here and wherever applicable, the statistical weight of each snapshot is derived from the steady state of the final network model (see Construction of Markov Model and sections S1.3.2–3). Two cartoons[28] of structures featuring particular values of segment distances are added to each panel (chain coloring as in Figure 1B with the additional modification that the segment in question is highlighted in magenta for all chains). Standard deviations across 1000 bootstrap samples of size 500 give an indication of statistical errors for the A–B and B–C interfaces. These symmetric error estimates are plotted as shaded areas. A random sample of 500 points covers ~0.01% of the data and draws from at most ~0.17% of the individual trajectories.

This is unlikely to be the case as shown in Figure S1. While segment distances are often correlated with COM-d at large separation of these observables, the same is not true at short separation. In particular, many different values of segment distances can map to the same value of COM-d and *vice versa*. As we will see below, these different structures can be separated by large kinetic barriers; thus, they cannot be expected to relax in umbrella sampling. The presence of many representative, docked conformations that can all be accessed by spontaneous fluctuations suggests that the onset of template-like order for the monomer is a late event in elongation. Disordered docking is consistent with the fact that Aβ monomers bind reversibly to large, linear aggregates irrespective of their structural maturity.[48] As an aside, this disorder prevents the PIGS heuristic from efficiently diversifying the conformations of chain A further. The effect is manifested in a drop in reseeding rate (Figure S2), which motivated adjustments of representation (Table S2).

Overall, Figure 2 suggests that LVFF and β2 in particular prefer to remain closely associated with chain B of the fibril template, albeit in predominantly nonnative arrangements. For CT and linker, the B–C interface is sometimes broken instead of the A–B interface, a process that would have been quenched by positional restraints on chain B. Conversely, β1 and Loop appear to be able to dissociate more rapidly. The importance of CT, LVFF, and β2 for monomer binding and, by extension, aggregation is in accordance with their hydrophobicity and consistent with many experimental studies mutating residues in Aβ, most clearly in Wurth et al.[63] It may be conjectured that the dramatic changes occurring at the A–B interface are merely the result of spontaneous rearrangements of the assembly. In order to dispel this notion, Figure 2 also shows the data for the other three interfaces. With the exception of B–C (CT and linker, see above), which is a consequence of the unlocking of chain A (e.g., bottom cartoon in Figure 2E), these interfaces do not appear to undergo significant changes, indicating that the pentameric assembly is sufficiently stable on the simulation time scale. The spontaneous relaxation that does occur at the pentamer level is illustrated in Figure S3 by a juxtaposition of the NMR structure and its equilibrated simulation equivalent. It involves an increase in twist and a contraction of the linker segment, likely in response to M35 being reduced, to sequester more hydrophobic surface area from solvent, similar to literature observations.[64]

Since we model both the N-termini and the solvent explicitly, it is useful to summarize their behavior as well. Similar to the ordered parts of chains B–E, there is no sampling enhancement for the N-termini in any of the chains. However, there is also no reference state. Our trajectories are too short in continuous time ($\leq$60 ns) to sample the configurational space of all N-termini well, and this is manifest in the sporadic interaction patterns seen in Figure 3. While generally extended and free of secondary structure (Figure S4), these segments participate in all conceivable interactions, i.e., they can bind each other (chains A vs C), collapse partially (chain E), or make interactions with the ordered template (chains B vs D), as seen in Figure 3. By integration, we find that the nonlocal contacts formed by the N-termini feature prominently positions F4, R5, and Y10 and the stretch $V_{12}HHQ_{15}$, which is predisposed toward intermolecular contacts on account of the template. This mix of aromatic–hydrophobic and salt bridge interactions (R5 interacts with both exposed negative charges on the ordered part, viz., E22 and the C-terminus) shields the surface of the protofibril somewhat from solvent.

From the analysis of solvent coordinates, we did not detect noteworthy phenomena involving counterions. The relaxed protofibril (Figure S3) seems to possess cavities, however, and we performed a limited analysis of water density inside the structures. Figure 4A,B shows visualizations for data collected for relatively homogeneous ensembles of locked states based on the two different starting structures. These two alternative conformations differ both in internal water content and in a salt bridge involving the N-terminus of chain D (see section S1.1). Figure 4A,B provides evidence that the internal salt bridges involving D23 and K28 are partially solvated, that the water channel connects with the bulk, and that any memory of the solvation difference in the starting structures is lost entirely. The combined data in Figures 2, 3, and 4A,B suggest that the initial modeling of the N-terminal segments, the choice of Gaussian well potentials for the stabilization of chains B–E, and the force field are adequate. Chains C–E form a well-defined template even though the well potentials influence only intramolecular degrees of freedom directly. As a result, any bias acting on the interfaces is indirect and weak. We are thus confident that the events observed for chain A, which extend toward chain B, are low likelihood events that capture long time scales. In the following, we turn to Markov state models in order to corroborate this statement and to quantify the dynamics at equilibrium.

Construction of Markov Model. Because we are studying a disorder-to-order transition, the number of relevant states is unknown and potentially large. It is thus essential to use a fine enough grouping to partition the data. The grouping we settled

DOI: 10.1021/acs.jctc.7b00662
J. Chem. Theory Comput. 2017, 13, 5117–5130

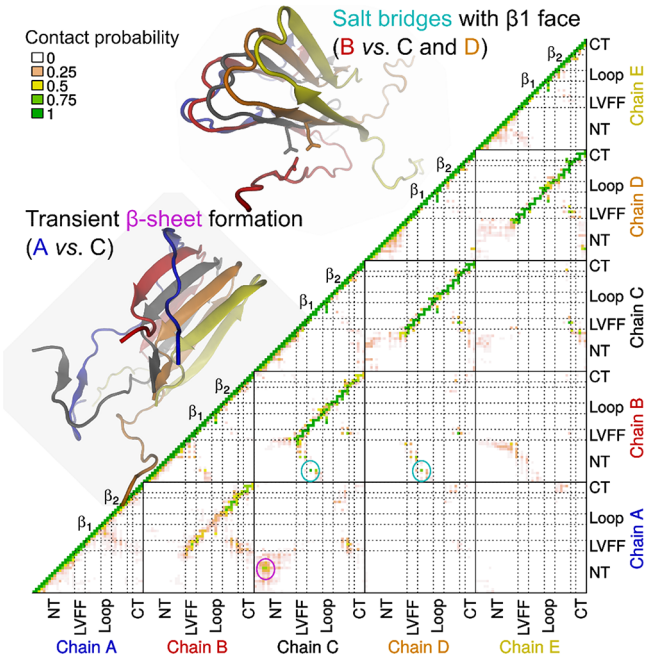

Figure 3. Contact map for the entire pentameric assembly. Two residues are defined to be in contact if their minimum pairwise interatomic distance is below 3.5 Å. Each square delineated by solid lines contains an *inter*molecular contact map for a specific pair of chains, and each triangle contains the *intra*molecular map for a given chain. Dashed lines delineate all seven regions of the peptide indicated in Figure 1D, which are labeled. Due to space reasons, the labels for $\beta 1$ and $\beta 2$ appear on the diagonal rather than on the sides. Contact probabilities are indicated by color (see legend, top left) and were calculated across the entire data set. The dominant pattern highlights the interpeptide, in-registry parallel β-sheet architecture (neighboring chain contacts parallel to the diagonal). Somewhat counterintuitively, the contacts between top and bottom strands, which show up as characteristic patterns orthogonal to the main diagonal, are not pronounced at this threshold level either within the same monomer or with respect to the neighboring one (the latter being stronger). Two cartoons are added that highlight two types of sporadic interactions as indicated (see text). The corresponding contacts are indicated by the colored circles.

on used all in-registry $C_\alpha - C_\alpha$ distances for residues 17−42 and selected intramolecular distances as coordinates (section S1.3.2 and Table S3) and a tree-based clustering algorithm known to yield networks that preserve kinetic information well.[66] We cross-checked the clustering against an alternative distance metric based on absolute coordinates and found that the partitioning is robust with respect to the metric in use (Figure S5). Figure S6 shows results for the implied time scales of models at different resolutions. These time scales are in the mid−μs regime. Using Figure S6, we chose 0.7 Å as the spatial resolution, and the resultant network contains ∼25 000 states. A lag time of 200 ps was deemed appropriate for the transition matrix, and we decided to superpose all transitions with this time lag (the so-called sliding window or SW approach). In addition, the count matrix, **C**, was symmetrized by setting the smaller element in each $C_{ik} - C_{ki}$ pair to the larger of the two values. This simple imposition of detailed balance by symmetrization provides results that are fundamentally similar to those from a statistical procedure that imposes detailed balance in a way that maximizes the likelihood of **C** under certain assumptions[67] (see Figure S7). The steady state of the network we ultimately chose served to calculate statistical weights for snapshots in simple analyses such as those in Figures 2 or S1. This procedure was followed consistently throughout.

As a test of robustness, we studied the impact of truncating the data in half. The first half of the data contains only PIGS simulations that all originated from the same starting structure. In the second half, we added also canonical MD simulations from various starting points (Table S1) and additional PIGS runs from a modified starting structure. This was done to assess the impact of potential long-lived features not directly influenced by PIGS (salt bridges formed by N-termini, water inside the fibril). The results of this crude subsampling approach are encouraging in that the addition of the second half does not seem to influence the implied time scales strongly (Figure S8). The mutual overlap in terms of shared clusters between all "first generation" PIGS runs, i.e., between the six replicates starting directly from the two alternative, NMR-derived structures, is another indicator of robustness (Figure S9). Finally, the water distribution converges between these two starting structures (Figure 4A,B), highlighting that at least some of their properties are inconsequential.

The derived Markov model allows us to extract rates for any process representable in it by means of transition path theory.[57] Briefly, we computed committor probabilities (p_{fold} values) for transitions between a representative set of fibrillar states and interesting (far away) docked states of chain A. The net probability flux and rates between states can be computed using this information. The net flux can be decomposed into a set of reactive pathways,[57] which relies on a heuristic. Here, we deviate from other works[44] and choose a decomposition that is able to represent the properties of the flux network more faithfully (section S1.3.6). As mentioned above, the fully dissociated state is not represented in our network, and we thus analyze different *locking pathways*. Clusters defining the homogeneous fibrillar state were selected based on a consensus approach applied to the first half of the data (blue in Table S1), and the resultant centroids are shown in Figure S10. Alternative locked conformations have very high p_{fold} values, suggesting that the precise choice is not crucial (e.g., the simulation structure in Figure S3 is from the second half of the data and has a p_{fold} value of 0.98). A set of three docked states, termed D1−D3, was identified based on visual inspection and low-dimensional order parameters. Side-by-side comparison in Figure S11 reveals that they are notably different from each other. Of course it would have been possible to select more and different states, but, as we show below, the pathways connecting the states D1−D3 to the fibrillar states cover most of the space our simulations explored.

Properties of Different Locking Pathways. Figure 5 shows the results for the net rate analysis mentioned above for locking and unlocking pathways. The net rates are shown in Figure 5A,B for both cases. Locking and unlocking rates sample intervals of $6-11 \times 10^{-2}$ and $3-6 \times 10^{-2}$ μs^{-1}, respectively. The narrow ranges and the lack of overlap in Figure 5B suggest that this is a statistically robust result given that the ranges provide error estimates from subsampling where each circular point relies on only ∼1% of the counts in **C**. The observation that the unlocking rates are lower by a factor ∼1.5−4 for individual trajectories (the SW ratio is ∼2) is a second very important and not at all trivial result given that the PIGS simulations naturally follow the *unlocking* process in forward

DOI: 10.1021/acs.jctc.7b00662
J. Chem. Theory Comput. 2017, 13, 5117−5130

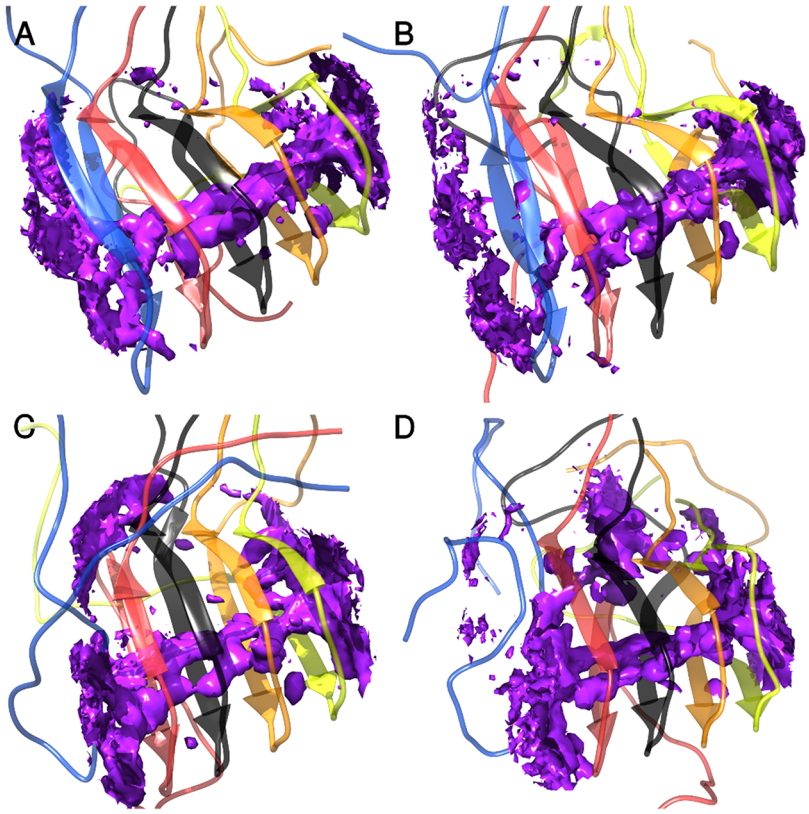

Figure 4. Visualization of protofibril−internal water molecules. Solvent coordinates were stored at a lower time resolution (140 and 350 ps, depending on the run) and were available only for the conventional sampling runs performed with GROMACS (Gromacs, Gromacs*, Gromacs0, and Gromacs21 in Table S1). After alignment based on a subset of C_α atoms from chains C and D, average density maps were computed for the water molecules alone. Densities were accumulated on cubic voxels of $(0.5\ \text{Å})^3$ using linear interpolation and 2000−5000 snapshots for each panel. The isocontour surfaces enclose an average water density >0.8 g/cm^3 and are shown in purple. They were computed and rendered by UCSF Chimera, Version 1.9,[65] in conjunction with the Persistence of Vision Pty. Ltd. (2004) Raytracer (http://www.povray.org/). Only density values associated with grid cells within 5.5 Å from *ad hoc* selected atoms within the interior of the pentamer are displayed for better clarity. The cartoon representations of the pentameric assembly were chosen as the centroid of the largest cluster of a clustering analysis performed on the individual conventional MD runs. (A) Gromacs. (B) Gromacs*. (C) Gromacs0. (D) Gromacs21. Comparison of the individual panels elucidates that there is a persistent water channel immediately adjacent to the D23−K28 salt bridges, which is connected to the bulk. The difference in starting structures with respect to internal solvation further away from the turn (see section S1.1) is no longer apparent (A vs B).

time. Experimentally, the ratio of locking and unlocking rates has been reported to be ∼10 for the rate-limiting step.[68]

The net locking rate for a joint state including D1−D3 (Figure 5A,B) is also decomposable into three similar rates of the same order of magnitude when D1−D3 are treated separately (Figure 5C,D). The slow time scale for all three cases indicates that D1−D3 are chosen appropriately given the data. Visual inspection of the trajectories suggests that the main kinetic bottleneck is the transfer of hydrophobic contacts from non-native to in-registry intermolecular arrangements. This is illustrated in Movies S1, S2, and S3, which show the series of spontaneous fluctuations that gave rise to D1−D3, respectively. A final important point is that all determined rates are much lower than what is covered by continuous trajectories in either our or others'[43,44] data sets.

To understand how much of our data set is represented by the ensembles of transition paths constituting the bulk rates reported in Figure 5, we utilize several principal component (PC) projections applied to the same distance-based representation used for clustering (Table S3). The projections in Figure 6 reveal two very important results. First, the space covered is almost fully explored by the pathway ensembles. Second, the overlap between the different pathways is generally small, thus suggesting that the results in Figure 5C,D regarding the similarity of time scales are not just a trivial result of describing the same pathway. Interestingly, there appear to be different numbers of on-pathway clusters for the locking of D1−D3 in these projections. Furthermore, the appearance of a broad envelope of clusters with comparable flux values for each docked state hints at a high level of redundancy in pathways for an individual locking transition. These last two features are expected in disorder-to-order transitions. We next consider individual docked conformations to illustrate these results structurally.

The first docked conformation, D1 (see Figure 7A), is characterized by retaining as its major intermolecular contact a non-native interaction of LVFF of chain A that is inserted into the interstrand interface of chain B. β2 and CT form a disordered globular conformation similar to that predicted by prior work on monomeric Aβ42.[33,34] This type of docked conformation is largely consistent with the dominant pathway predicted by Han and Schulten,[44] who identified LVFF as the most likely sequence stretch to engage first during docking at both even and odd ends. Figure 7B−D details the evolution of D1 toward the locked state. The distance and secondary structure data both reveal that LVFF remains non-native during

DOI: 10.1021/acs.jctc.7b00662
J. Chem. Theory Comput. 2017, 13, 5117−5130

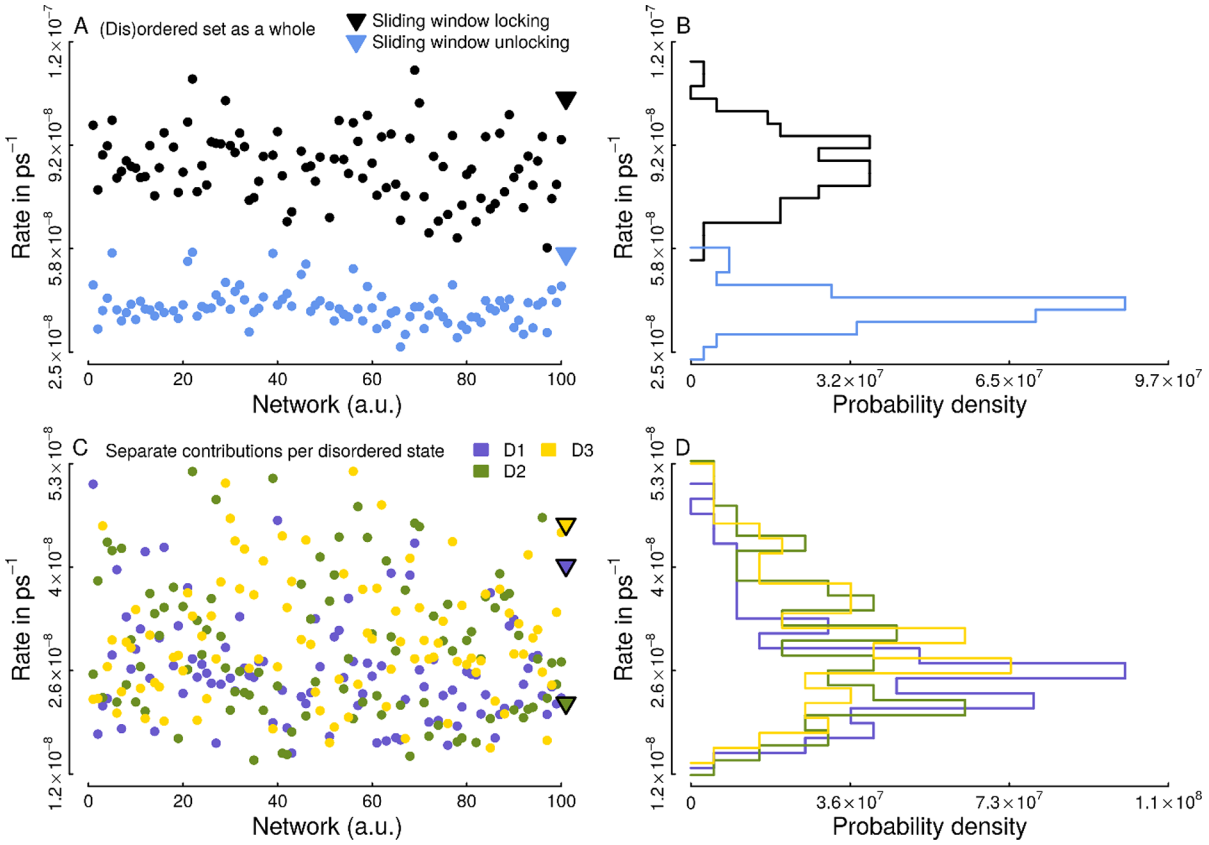

Figure 5. Rates of locking and unlocking and their robustness. (A) For the set of D1−D3 (Figure S11), we computed flux-based rates into the set of fibrillar states (Figure S10) from committor probabilities.[57] With the chosen lag time of 200 ps and a trajectory saving interval of 2 ps, we could create 100 individual networks (circles) in addition to the SW network (triangles). All 101 locking (black) and unlocking (blue) rates are shown, and their mutual similarities indicate the robustness of this result. (B) Histogram of the rates in A. (C) The same as A but plotted separately for D1−D3 and only for locking rates by means of eq S3 (additive fluxes). (D) The same as B but for locking rates only and D1−D3 separately.

the entire locking process, whereas the first segment to "lock down" is actually β2. The projected transition state ensemble near p_{fold} values of 0.5 suggests a concerted "threading" of part of β1, β2, and CT as the kinetic bottleneck. Figure 7B−D shows a superposition of pathways that agrees well with the single strongest pathway (Figure S13). In addition, this network-derived progression of events seems to also coincide with the geometrically continuous pathway extracted from the raw simulation data. This point is made by the p_{fold} annotation in Movie S1.

As mentioned, locking of D1 features LVFF in changing nonnative arrangements until very late. For high values of p_{fold}, this arrangement is actually shared by D2 and D3 and corresponds to an initial relaxation of the locked state seen in most of the simulations. Specifically, LVFF of chain A partially slides toward the β2 face, which allows a deeper insertion of F19 into the intrasheet interface accompanied by better hydrophobic packing. Comparatively fast relaxation of this type suggests that the fibril tip is likely to be partially disordered, a result that is consistent with prior studies that show considerable loss of structure for smaller assembly sizes upon relaxation in solution.[64]

D2 (see Figure 8 and Movie S2) demonstrates a fundamentally different locking pathway from D1. Here, CT and a small part of β2 are the only segments at in-registry distances from chain B in the docked state. Conversely, the other regions including LVFF are fully dissociated. Intriguingly, the CT of chain B is actually detached from chain C, which gives rise to the non-nativeness at the B−C interface discussed in the context of Figure 2E−F. Together, CT and linker of chains A and B are bound to the hydrophobic protofibril surface, i.e., to the β2 strands of chains C−E, which causes an additional deformation of the entire pentamer. This result is intriguing for three reasons. First, it provides evidence that disorder can extend to more than one monomer. Second, it suggests that a monomer can not only dock to this interface[48] but also slide into place upon binding. We screened the trajectories and found a more extreme version of D2 (Figure S14) that makes this mechanism seem plausible. Third, the fact that the CT of chain B detaches from chain C provides a direct mechanistic clue for why Aβ42 may elongate faster than Aβ40. In essence, the CT of the last locked monomer (or monomers) could serve as an anchor "catching" incoming monomers as described (on a geometrically larger scale) for IDPs.[70]

In terms of dominant pathways, Figure 8 identifies as a late event that the CTs of A and B migrate from the lateral interface to the in-registry position and associate with C. Both here and in Movie S2, there is not as obvious an event associated with the presumed transition state ensemble as for D1. The binding of LVFF and the adjacent residues in β1 to the front of the fibril is an early event, and part of the rate-limiting behavior seems to come from the CT interfaces between both A−B (Figure 8C) and B−C (Figure 8D) and/or the loop region and the remainder of β1. Figure S15 reveals that there are two barriers of comparable height, which partially explains the absence of a well-defined transition state ensemble.

DOI: 10.1021/acs.jctc.7b00662
J. Chem. Theory Comput. 2017, 13, 5117−5130

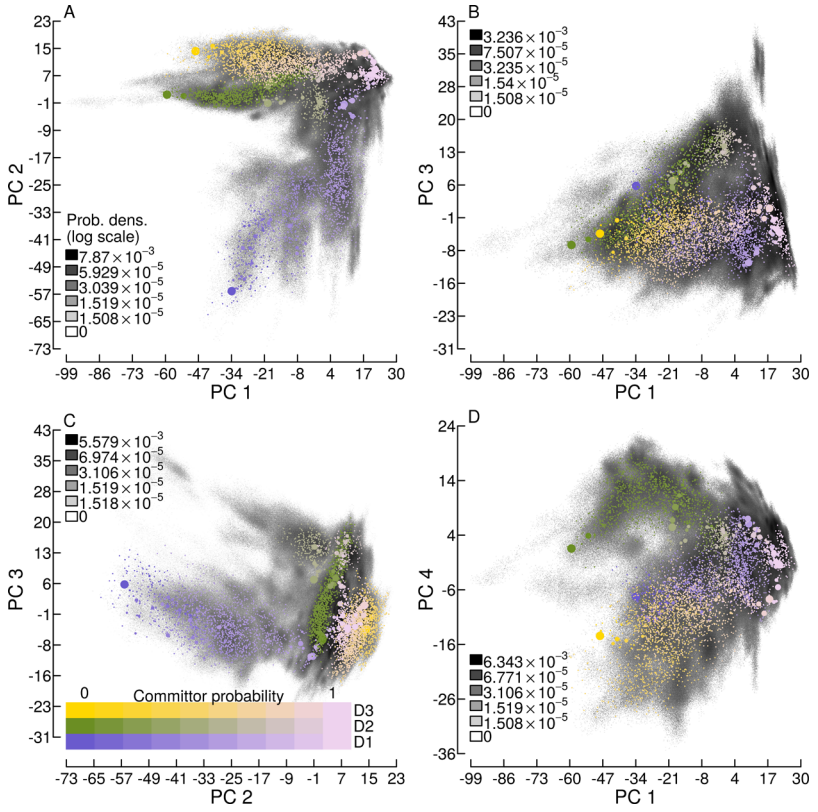

Figure 6. Phase space coverage of locking pathways. We computed PCs for the entire data set and transformed the raw data. From the pathway decomposition analysis described above and in section S1.3.6, we obtained clusters with contributions to the reactive flux for D1−D3 (same color code as in Figure 5). (A) The steady-state-weighted and snapshot-based histogram of the 2D projection onto the two PCs with largest variance is shown in gray. Cluster centroids of clusters with non-zero flux contributions are added as colored circles with circle diameter proportional to reactive flux. The flux decomposition mandates a monotonic increase in p_{fold} (i.e., no pathways that backtrack are evaluated). Colors converge toward the fibrillar state which is shared by all pathways. (B) The same as A for PCs 1 and 3. (C) The same as A for PCs 2 and 3. (D) The same as A for PCs 1 and 4.

Lastly, D3 populates a large unique area of phase space according to Figure 6. It shares with D2 the detachment of the B−C interface at CT, although here they are solvent-exposed. Compared to D1 and D2, D3 retains the largest amount of native contacts as parts of β2 and CT are formed and fully in-registry throughout (Figure S16B,C). Similar to D2, the locking pathway ensemble suggests that formation of the B−C interface of CT is a late event and that the rate-limiting step is more likely related to the transfer of intramolecular contacts from LVFF of chain A toward intermolecular ones with chain B (see Movie S3). This is supported by Figure S17, which highlights a rugged free energy landscape with multiple relevant barriers pertaining to the rearrangement of the A−B interface for LVFF and β1. While there could be and likely are any number of additional docked conformations and associated locking pathways, we discuss below a number of conceptual properties of the locking process that are already captured by the current data set.

DISCUSSION

Above we have presented and analyzed a complex data set from atomistic simulations describing the dynamics of the terminal monomers in a gently stabilized model fibril of Aβ42. The data reveal locking transitions from various docked conformations on the high microsecond time scale. We now discuss how our findings may transfer to the elongation of Aβ fibrils *in vitro* and *in vivo* and what they add to prior computational studies.

Hydrophobic Interactions Are Likely To Control Both Docking and Locking Rates. In our simulations, the terminal monomer at the odd end often engages in non-native interactions with the rest of the fibril that are driven by hydrophobic contacts. As is well-known, Aβ is an unusually hydrophobic IDP and adopts globular conformations (micelle- or premolten globule-like)[34] in solution, which fail to completely shield all hydrophobic patches.[71] Our data reveal that exposed hydrophobic patches indicated experimentally for example by ANS binding[72] are very likely responsible for docking. A prominent candidate is LVFF as in the docked state D1 (Figure 7A), which is in congruence with many mutational studies and the main pathway of Han and Schulten.[44] More than the breakage/formation of β-hydrogen bonds, the exchange of contacts, for example from intra- to intermolecular ones, appears to encode the slow steps in the locking pathways (Figure S18). Our setup allows the penultimate monomer to become partially non-native (Figure 2E-F), and this is highlighted clearly by D2 (Figure 8). Being an indirect consequence of the conformational diversification for chain A, this observation suggests to us that the tip of a protofibril in solution should be partially disordered. This disorder is likely driven by the need to sequester hydrophobic interfaces from solution, and it may well involve several monomers. The observed negative temperature dependence of the free monomer concentration at quasi-equilibrium supports the crucial role of hydrophobic interactions in elongation.[25]

DOI: 10.1021/acs.jctc.7b00662
J. Chem. Theory Comput. 2017, 13, 5117−5130

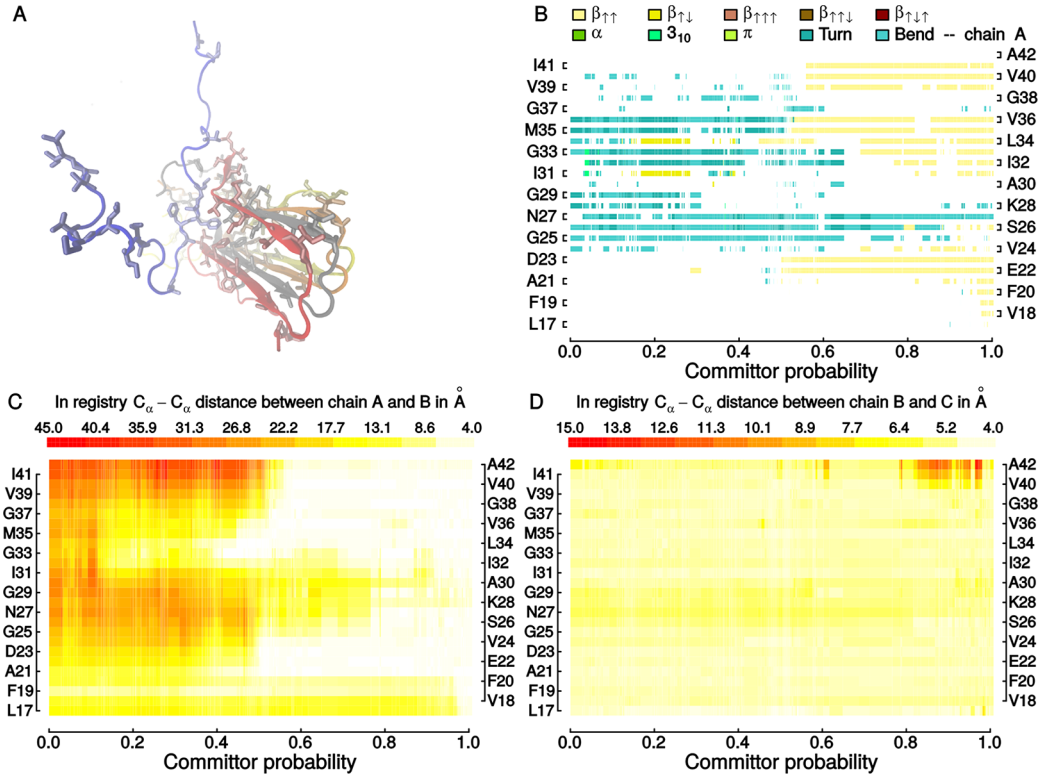

Figure 7. Structural progression of locking pathway for D1. (A) Cartoon representation of D1. Panels B–D plot different properties as color maps resolved by p_{fold}. Pathways are decomposed as described in section S1.3.6, and there is no single pathway with very large weight. To display the data globally, values for relevant cluster centroids are simply plotted as a function of p_{fold}, and colored blocks extend toward the next highest p_{fold} value. Relevant clusters are identified as those carrying at least 1% of the flux encoded by the (single) strongest reactive path. p_{fold} values are of course spaced unevenly, and Figure S12 provides a complementary plot showing all clusters with a scale on the *x*-axis proportional to the steady-state population. (B) DSSP[69] annotation of secondary structure assignment for chain A. (C) In-registry distances between C_α atoms at the A–B interface. (D) The same as C for the B–C interface.

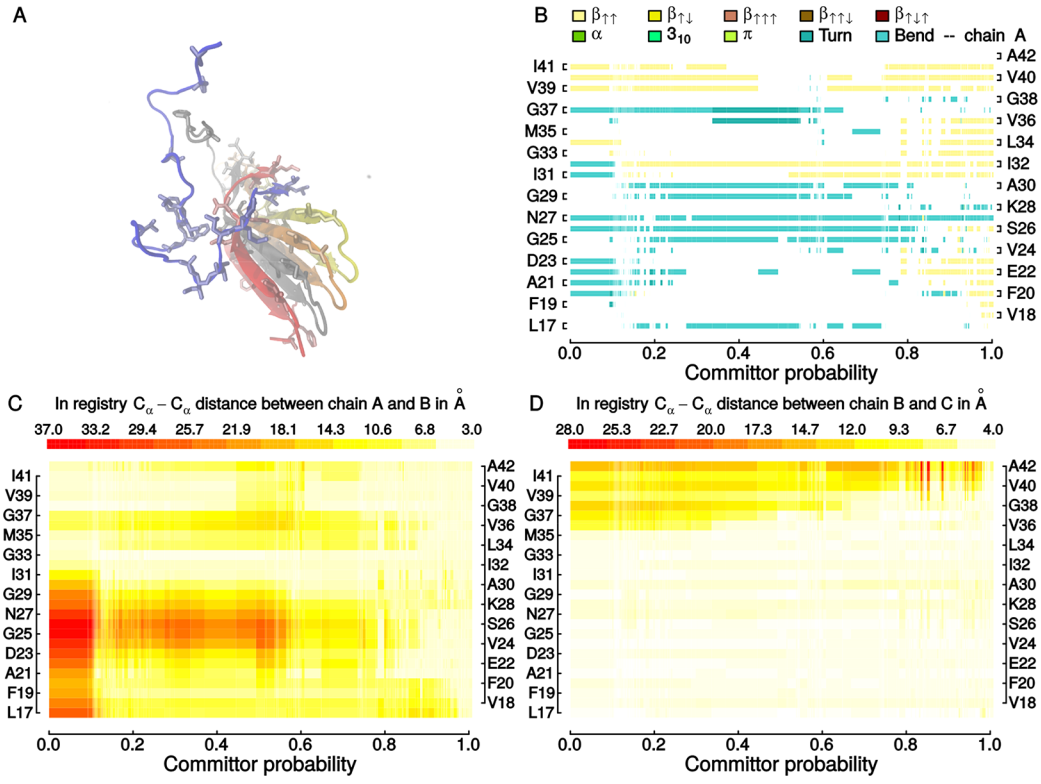

Figure 8. Structural progression of locking pathway for D2. See caption to Figure 7 for details (complementary plot in Figure S15).

DOI: 10.1021/acs.jctc.7b00662
J. Chem. Theory Comput. 2017, 13, 5117–5130

There Is No Evidence for Slow Processes Involving Critical Water Molecules. We could not store water coordinates at the same time resolution as the peptide, and only a limited analysis on homogeneous stretches of D1, D2, and the two alternative starting structures is shown in Figure 4. As alluded to above, water relaxes to a single channel that partially solvates the internal salt bridge in the locked state (Figure 4A,B), consistent with expectations from 2D-IR experiments on ordered Aβ fibrils.[73] The particularity of possessing a mix of wet and dry nonlocal contact interfaces implies the presence of fibril−internal water wires that have also been characterized for aggregates of shorter peptides[74−76] and other Aβ polymorphs.[77] The same analysis for relatively homogeneous ensembles of D1 and D2 in Figure 4C,D reveals that (i) non-native conformations of chain A do not cap (seal off) or otherwise strongly perturb this water wire, which would be entropically unfavorable; (ii) water can flow into additional protofibril-internal cavities if the assembly deforms more strongly. Both processes at most suggest relaxation processes involving water, but our stored data provide no evidence that (de)wetting transitions slow down locking pathways beyond the simple mechanism of controlling the exchange of hydrophobic contacts.

Hairpin-Like Intermediates Do Not Occur toward the End of Locking Pathways. In all proposed structures of Aβ fibrils, monomers adopt conformations featuring strand-loop-strand motifs, although the numbers and positions of the turn(s) can vary. For example, a very recent solid-state NMR structure[78,79] of Aβ42 features two turns and an S-shaped monomer arrangement. Conversely, the single strand−loop−strand architecture in our study (e.g., Figure 7B) is inherited directly from the Lührs et al. structure.[58] Distinct from these architectures, an intermediate has been postulated that is a β-hairpin where β1 and β2 form *intra*molecular hydrogen bonds. In solution, Aβ's β-content is low,[20] and the mean architecture is globular.[34] Recent simulations have shown that similar hairpins are observed across force fields in Aβ42 dimers with populations ranging from 1 to 13%.[37] Gurry and Stultz[43] discuss hairpins as obligate intermediates for fibril growth, whereas in our data set the β-hairpin conformer shown in Figure S14 is the exception rather than the rule. For example, D1 does not form any significant intramolecular hydrogen bonds during locking (Movie S1). Han and Schulten[44] also observed hairpin intermediates, albeit less frequently and with shorter strands. We propose here that it is primarily the intra- to intermolecular transfer of the predominantly hydrophobic contacts rather than β-hydrogen bonds that are the more likely rate-limiting events in locking (Figure S18). An additional deviation from these prior works is that we did not record (re)binding events of LVFF or β1 in an antiparallel fashion, which we think would be opposed by the N-termini.

N-Terminal Segments Can Shield the Protofibril. As described in the Results and Figure 3, the N-terminal segments may play an important role in protecting both lateral and terminal interfaces of protofibrils transiently. Movies S1, S2, and S3 demonstrate that the tails are disordered and prefer interactions with the β1 interface relative to the β2 one, which are most likely favored entropically. It is consistent with our data that the N-termini therefore play two important roles. First, they act as entropic brushes, i.e., any lateral association must overcome an entropy penalty due to restrictions of the conformational space of the N-termini. Second, they can make transient contacts with interaction hot spots on the fibril surface, e.g., V18/F20 or E22. A shielding role for the N-termini fits well with results for the D7N and H6R familial mutations, suggesting a specific acceleration of fibril elongation.[50] As both mutations make the N-terminus more positively charged, it is conceivable that the N-termini are increasingly directed toward the laterally exposed side chains of E22 in the ordered part and that the tips become less protected in the process. Conversely, the protective A2T mutation[52] does not share the same property, does not pertain to a residue of particular interest in Figure 3, and shows only a mild alteration of Aβ42 elongation kinetics *in vitro*.[80] Other cases may be more complicated, for example, the A2V mutant.[81] Of course, in many mutants there can be a substantial impact of an N-terminal substitution on the monomeric and oligomer ensembles, which is not resolved by our study but was highlighted by molecular simulations.[82,83]

Nonspecific Lateral Association of Monomers Can Shield Protofibrils as Well. The protofibril structure inferred from solution NMR (see Figure 1B) is comparatively stable in simulations (Figure 2) and derived from a solution species that is lacking compact interfaces between protofibrils.[58] It does, however, appear to possess solvophobic interfaces: there should be driving forces to cover both the large lateral (V18, F20, I31, M35, V39, and I41 are all solvent-exposed) and small terminal (F19 at the even end) hydrophobic patches. Moreover, the side chains of E22 should, aside from pK_a shifts, be compensated with positive charges. The N-termini of locked monomers likely contribute to both effects. In D2 (Movie S2 and Figure 8), we see that the β2 face, which is least protectable by the N-termini (Figure 3), is prone to nonspecific binding events by docked monomers, which was observed experimentally for large, partially ordered aggregates[48] and for fibrils.[84] Evidently, monomers retain significant affinity toward 2-fold fibrils although it is likely lower than for the protofibril model we used, which lacks the contacts between protofibrils implied by the 2-fold arrangement. Docked conformations of the type seen in Figure S14 may solubilize (proto)fibrils and give rise to the observed noninteger values for the number of monomers per repeat unit.[85] Depending on the relative kinetics, sliding along the surface could also contribute to the net elongation rate. Gurry and Stultz[43] observed a conceptually similar "rolling" motion for Aβ42 that occurred along the loop surface, however.

Impact of the Choice of Template and the Lack of Contacts between Protofibrils. Our study uses the protofibril model of Lührs et al.[58] Solid-state NMR and cryoEM structures suggest that the coalescence of protofibrils leads to assemblies in which more of the hydrophobic surface area can be buried,[78,79,86] although structures with large internal solvent channels have been determined as well.[87,88] Most of these structures involve a larger number of turns per chain and allow only for a limited number of intermolecular hydrogen bonds when compared to the model of Lührs et al.[58] Because the lateral hydrophobic interfaces are better sequestered, it is fair to predict that lateral associations of additional monomers would become less likely (see previous paragraph). Conversely, salt bridge interactions with the N-termini are likely enhanced as both E22 and D23 can be exposed.[78,79,89] Both effects are consistent with an increase in the relative associativity of the fibril tips, i.e., a quaternary structure of this type is able to rationalize how large linear aggregates form in solution. Because the secondary structure content in these structures is often lower to begin with, we predict that our conclusions regarding tip disorder and the role of hydrophobic interactions would be

DOI: 10.1021/acs.jctc.7b00662
J. Chem. Theory Comput. 2017, 13, 5117−5130

similar, and this is part of ongoing work. It should not be forgotten that Aβ fibrils, in particular Aβ42, are polymorphic,[4,26,90] and conclusions holding across polymorphs are inherently more interesting than polymorph-specific ones.

Relationship of Locking Rates to Experimental Measurements of Fibril Growth. Experimentally, fibril elongation is a slow process, but the actual rate of growth varies considerably with a number of factors. These include the difficulty in controlling the number of growing ends in ensemble experiments (due to ongoing primary and secondary nucleation)[91,92] as well as surface attachment, solution conditions, fibril polymorph, etc. Reported elongation rates can vary by several orders of magnitude for Aβ42.[26,68] In addition, it is not straightforward to interpret the observed rates given that successful fitting does not *per se* imply a mechanistic validation.[49,93] Even when selecting experimental numbers favorably, individual rate constants inferred *in silico* tend to be too large by one to several orders of magnitude.[45,56] Due to the volatility of rate estimates from either end, it does not appear meaningful to attempt to corroborate simulation results by matching rates. Instead, we, above and below, connect our results to a number of qualitative and robust experimental observations, in particular regarding hydrophobic interactions, the stop−go nature of single fibril growth, lateral interactions with the fibril, etc.

Structural Asymmetry Required for Growth Asymmetry Persists. Lührs et al.[58] argued for the odd end as the fast growing one based on the inhibitory activity of N-methylated peptides, and this is the protofibril end investigated in this study. Han and Schulten[44] obtained the opposite result with the same structure employed as a relatively rigid template and with the N-termini truncated. In our simulations, we observe a readily accessible, non-native conformation of LVFF at the odd end, which slides to and inserts at the front (e.g., Movie S2). The β2 hydrophobic interface of the pentamer is partially sequestered by the linker region contracting, which is also a relatively fast process (Figure S3C,D). We do not observe larger spontaneous rearrangements at the even end (chain E) where sampling is not enhanced by PIGS except that the salt bridge to chain D is broken occasionally (Figure S19). These results suggest that both fibril ends can form disordered tip structures with differing properties. In experiments, fibrils show similar stepwise growth at both ends, albeit with different rates.[26] Ultimately, these differences must be propagated from a fundamental asymmetry in the fibril, and this asymmetry, discussed at length by Lührs et al.,[58] is never lost in our simulations. Figure S20 demonstrates this point by quantifying the distribution of the stagger of the β1 and β2 sheets along the fibril axis.

Implications for the Dock-and-Lock Mechanism of Aβ Fibril Elongation. Our simulations offer an atomistic view of the elongation process that in coarser terms is similar to that discussed in Qiang et al. for Aβ40.[25] We hypothesize that monomers at the end of the growing fibril are less ordered than those in the middle and constitute a capping structure. Locking happens progressively inside the cap, and this is the rate-limiting step. The presence of additional docked monomers is important because locking involves the formation of the correct intra- and intermolecular interfaces along with (de)solvation events. The cap is partially disordered and exposes different interfaces, which control the rates of monomer binding and unbinding. We believe a steady state is reached during productive growth because these rates become equal rather than vanish. Occasionally the cap switches to a growth-incompetent state, and this gives rise to the observed arrest phases in single fibril observations of elongation. The incompetent state could correspond to a number of kinetically trapped states at the level of the entire cap. At all times, reversible binding of soluble Aβ (and possibly other species) to the protofibril surface modulates the monomer pool available for docking and lowers the likelihood of growth in additional dimensions. These interactions are entropically favored as they release solvent and are able to preserve the monomer's disorder. The fact that, outside of arrest phases, the growth of single Aβ fibrils occurs with an almost constant rate suggests that the locking rate is weakly dependent on cap conformation and largely determined by the structure of the template.

Conclusions and Outlook. Computer simulations increasingly complement experimental data, which is of particular importance for systems that at least partially reside in disordered states. Conditional upon the solution NMR structure (Figure 1),[58] we here shed light on transient states likely to be encountered during Aβ42 protofibril elongation. With explicit solvent and a modern force field, a large ensemble of trajectories was used to construct a network model able to illuminate the disorder-to-order transition corresponding to conformational locking. We obtain a broad coverage of phase space (Figure 6) for the attaching monomer at the odd end from different docked states (Figure 7, etc.) that all lock with similar rates (Figure 5). Unlocking rates are consistently lower than locking rates, in agreement with expectation.

In the future, we hope to provide an even richer atomistic picture of fibril elongation through additional simulations, viz., by studying the even end of the protofibril (Figure 1B)[58] and by changing the reference model.[78,79] One of the ultimate goals will be to use the simulation data to inform a plausible kinetic model similar to what is described in the last section above. We will integrate such a model in order to produce synthetic experimental data, which will hopefully contribute to the resolution of some inconsistencies found in the literature. As an example, the simple dock−lock scheme predicts saturation (enzyme-like) kinetics for elongation with monomeric Aβ concentration, [M], because of the presence of a rate-limiting step that is independent of [M].[21,23,25] Unfortunately, the saturation regime has proven difficult to establish, and linear (quasi-first-order) dependencies have been observed even up to tens of micromolar Aβ concentrations.[94] This is despite the fact that the elongation rates in this regime appear to exceed fitted locking rates[68] while remaining orders of magnitude below an estimate of the diffusion-based on-rate obtained under similar conditions.[25,95] These results suggest that ongoing (secondary) nucleation events[91,92] mask the saturation regime of fibril elongation.

■ ASSOCIATED CONTENT

Supporting Information

The Supporting Information is available free of charge on the ACS Publications website at DOI: 10.1021/acs.jctc.7b00662.

Additional details on system setup (S1.1), simulation protocols (S1.2 and Tables S1 and S2), and data analysis (S1.3 and Table S3); additional results (Figures S1, S2, S4, and S18−S20), cartoons of locked and docked states (Figures S3, S10, and S11), complementary results for the different locking pathways (Figures S12−S17), and figures for demonstrating robustness and justifying

DOI: 10.1021/acs.jctc.7b00662
J. Chem. Theory Comput. 2017, 13, 5117−5130

choices made during analysis (Figures S5−S9 and S21−S22) (PDF)

Web-Enhanced Features

Movie S1: By tracing back the PIGS reseeding history, we extracted a geometrically continuous, time-reversed trajectory converting D1 to the fibrillary state. This concatenation of short trajectories has a net length of only ∼30 ns in simulation time, yet the process has an implied time scale in the high microsecond regime. The movie shows a view of the odd end (left) with hydrophobic residues as either sticks (top) or smooth surface (bottom). In addition, angled top and bottom views of the β2- and β1-side of the pentamer (right) are provided in surface representation. Coloring is by chain with chain A in blue. Visualization was done with VMD[28] and the Tachyon ray tracer. Perspective rendering with a depth-of-field effect and shadows is meant to enhance depth perception. Trajectory jitter was removed with a smoothing window of 40 ps applied to a saving frequency of 2 ps. The p_{fold} values indicated demonstrate that this path shares the same progression as the many pathways constituting the reactive flux for this transition (see Figure 7). Movie S2: The same as Movie S1 for D2. Movie S3: The same as Movie S1 for D3. Note that the movie is shorter because the concatenation of individual trajectories has a net length of only ∼15 ns in simulation time in this case.

AUTHOR INFORMATION

Corresponding Authors

*(A.C.) E-mail: caflisch@bioc.uzh.ch.

*(A.V.) E-mail: a.vitalis@bioc.uzh.ch. Tel/Fax: +41 44 635 5568/+41 44 635 6862.

ORCID

Amedeo Caflisch: 0000-0002-2317-6792

Andreas Vitalis: 0000-0002-5422-5278

Present Address

†(J.V.) Institute of Organic Chemistry and Biochemistry AS CR, v.v.i. Flemingovo náměstí 542/2, CZ-166 10 Prague 6, Czech Republic.

Notes

The authors declare no competing financial interest.

‡(M.M.) No current professional affiliation.

ACKNOWLEDGMENTS

This work was supported by a grant from the Swiss National Science Foundation (SNF #149897) to A.C. and by a grant from the Platform for Advanced Scientific Computing (PASC "Scalable Advanced Sampling in Molecular Dynamics") to A.V. and A.C.

REFERENCES

(1) Ross, C. A.; Poirier, M. A. What is the role of protein aggregation in neurodegeneration? *Nat. Rev. Mol. Cell Biol.* **2005**, *6*, 891−898.

(2) Jost, B. C.; Grossberg, G. T. The evolution of psychiatric symptoms in Alzheimer's disease: A natural history study. *J. Am. Geriatr. Soc.* **1996**, *44*, 1078−1081.

(3) Serrano-Pozo, A.; Frosch, M. P.; Masliah, E.; Hyman, B. T. Neuropathological alterations in Alzheimer disease. *Cold Spring Harbor Perspect. Med.* **2011**, *1*, a006189.

(4) Annamalai, K.; Gührs, K.-H.; Koehler, R.; Schmidt, M.; Michel, H.; Loos, C.; Gaffney, P. M.; Sigurdson, C. J.; Hegenbart, U.; Schönland, S.; Fändrich, M. Polymorphism of amyloid fibrils *in vivo*. *Angew. Chem., Int. Ed.* **2016**, *55*, 4822−4825.

(5) LaFerla, F. M.; Green, K. N.; Oddo, S. Intracellular amyloid-β in Alzheimer's disease. *Nat. Rev. Neurosci.* **2007**, *8*, 499−509.

(6) Hu, X.; Crick, S. L.; Bu, G.; Frieden, C.; Pappu, R. V.; Lee, J.-M. Amyloid seeds formed by cellular uptake, concentration, and aggregation of the amyloid-β peptide. *Proc. Natl. Acad. Sci. U. S. A.* **2009**, *106*, 20324−20329.

(7) Esbjörner, E. K.; Chan, F.; Rees, E.; Erdelyi, M.; Luheshi, L. M.; Bertoncini, C. W.; Kaminski, C. F.; Dobson, C. M.; Kaminski Schierle, G. S. Direct observations of amyloid β self-assembly in live cells provide insights into differences in the kinetics of Aβ(1−40) and Aβ(1−42) aggregation. *Chem. Biol.* **2014**, *21*, 732−742.

(8) Hardy, J. A.; Higgins, G. A. Alzheimer's disease: The amyloid cascade hypothesis. *Science* **1992**, *256*, 184−185.

(9) Wirths, O.; Multhaup, G.; Bayer, T. A. A modified β-amyloid hypothesis: intraneuronal accumulation of the β-amyloid peptide − the first step of a fatal cascade. *J. Neurochem.* **2004**, *91*, 513−520.

(10) Musiek, E. S.; Holtzman, D. M. Three dimensions of the amyloid hypothesis: Time, space and 'wingmen'. *Nat. Neurosci.* **2015**, *18*, 800−806.

(11) Mucke, L.; Selkoe, D. J. Neurotoxicity of amyloid β-protein: Synaptic and network dysfunction. *Cold Spring Harbor Perspect. Med.* **2012**, *2*, a006338.

(12) Knopman, D. S.; Jack, C. R.; Wiste, H. J.; Weigand, S. D.; Vemuri, P.; Lowe, V. J.; Kantarci, K.; Gunter, J. L.; Senjem, M. L.; Mielke, M. M.; Roberts, R. O.; Boeve, B. F.; Petersen, R. C. Brain injury biomarkers are not dependent on β-amyloid in normal elderly. *Ann. Neurol.* **2013**, *73*, 472−480.

(13) Iwatsubo, T.; Odaka, A.; Suzuki, N.; Mizusawa, H.; Nukina, N.; Ihara, Y. Visualization of Aβ42(43) and Aβ40 in senile plaques with end-specific Aβ monoclonals: Evidence that an initially deposited species is Aβ42(43). *Neuron* **1994**, *13*, 45−53.

(14) Kuperstein, I.; Broersen, K.; Benilova, I.; Rozenski, J.; Jonckheere, W.; Debulpaep, M.; Vandersteen, A.; Segers-Nolten, I.; Van Der Werf, K.; Subramaniam, V.; Braeken, D.; Callewaert, G.; Bartic, C.; D'Hooge, R.; Martins, I. C.; Rousseau, F.; Schymkowitz, J.; De Strooper, B. Neurotoxicity of Alzheimer's disease Aβ peptides is induced by small changes in the Aβ42 to Aβ40 ratio. *EMBO J.* **2010**, *29*, 3408−3420.

(15) Lomakin, A.; Teplow, D. B.; Kirschner, D. A.; Benedek, G. B. Kinetic theory of fibrillogenesis of amyloid β-protein. *Proc. Natl. Acad. Sci. U. S. A.* **1997**, *94*, 7942−7947.

(16) Hellstrand, E.; Boland, B.; Walsh, D. M.; Linse, S. Amyloid β-protein aggregation produces highly reproducible kinetic data and occurs by a two-phase process. *ACS Chem. Neurosci.* **2010**, *1*, 13−18.

(17) Nichols, M. R.; Moss, M. A.; Reed, D. K.; Cratic-McDaniel, S.; Hoh, J. H.; Rosenberry, T. L. Amyloid-β protofibrils differ from amyloid-β aggregates induced in dilute hexafluoroisopropanol in stability and morphology. *J. Biol. Chem.* **2005**, *280*, 2471−2480.

(18) Fändrich, M.; Meinhardt, J.; Grigorieff, N. Structural polymorphism of Alzheimer Aβ and other amyloid fibrils. *Prion* **2009**, *3*, 89−93.

(19) Tycko, R. Physical and structural basis for polymorphism in amyloid fibrils. *Protein Sci.* **2014**, *23*, 1528−1539.

(20) Riek, R.; Güntert, P.; Döbeli, H.; Wipf, B.; Wüthrich, K. NMR studies in aqueous solution fail to identify significant conformational differences between the monomeric forms of two Alzheimer peptides with widely different plaque-competence, Aβ(1−40)ox and Aβ(1−42)ox. *Eur. J. Biochem.* **2001**, *268*, 5930−5936.

(21) Esler, W. P.; Stimson, E. R.; Jennings, J. M.; Vinters, H. V.; Ghilardi, J. R.; Lee, J. P.; Mantyh, P. W.; Maggio, J. E. Alzheimer's disease amyloid propagation by a template-dependent dock-lock mechanism. *Biochemistry* **2000**, *39*, 6288−6295.

(22) Cannon, M. J.; Williams, A. D.; Wetzel, R.; Myszka, D. G. Kinetic analysis of beta-amyloid fibril elongation. *Anal. Biochem.* **2004**, *328*, 67−75.

(23) Ban, T.; Hoshino, M.; Takahashi, S.; Hamada, D.; Hasegawa, K.; Naiki, H.; Goto, Y. Direct observation of Aβ amyloid fibril growth and inhibition. *J. Mol. Biol.* **2004**, *344*, 757−767.

DOI: 10.1021/acs.jctc.7b00662
J. Chem. Theory Comput. 2017, 13, 5117−5130

(24) Kellermayer, M. S. Z.; Karsai, Á.; Benke, M.; Soós, K.; Penke, B. Stepwise dynamics of epitaxially growing single amyloid fibrils. *Proc. Natl. Acad. Sci. U. S. A.* **2008**, *105*, 141−144.
(25) Qiang, W.; Kelley, K.; Tycko, R. Polymorph-specific kinetics and thermodynamics of β-amyloid fibril growth. *J. Am. Chem. Soc.* **2013**, *135*, 6860−6871.
(26) Watanabe-Nakayama, T.; Ono, K.; Itami, M.; Takahashi, R.; Teplow, D. B.; Yamada, M. High-speed atomic force microscopy reveals structural dynamics of amyloid β1−42 aggregates. *Proc. Natl. Acad. Sci. U. S. A.* **2016**, *113*, 5835−5840.
(27) Nichols, M. R.; Moss, M. A.; Reed, D. K.; Lin, W.-L.; Mukhopadhyay, R.; Hoh, J. H.; Rosenberry, T. L. Growth of β-amyloid(1−40) protofibrils by monomer elongation and lateral association. Characterization of distinct products by light scattering and atomic force microscopy. *Biochemistry* **2002**, *41*, 6115−6127.
(28) Humphrey, W.; Dalke, A.; Schulten, K. VMD: Visual molecular dynamics. *J. Mol. Graphics* **1996**, *14*, 33−38.
(29) Fawzi, N. L.; Okabe, Y.; Yap, E.-H.; Head-Gordon, T. Determining the critical nucleus and mechanism of fibril elongation of the Alzheimer's Aβ1−40 peptide. *J. Mol. Biol.* **2007**, *365*, 535−550.
(30) Li, M. S.; Klimov, D. K.; Straub, J. E.; Thirumalai, D. Probing the mechanisms of fibril formation using lattice models. *J. Chem. Phys.* **2008**, *129*, 175101.
(31) Pellarin, R.; Caflisch, A. Interpreting the aggregation kinetics of amyloid peptides. *J. Mol. Biol.* **2006**, *360*, 882−892.
(32) Stine, W. B.; Dahlgren, K. N.; Krafft, G. A.; LaDu, M. J. *In vitro* characterization of conditions for amyloid-β peptide oligomerization and fibrillogenesis. *J. Biol. Chem.* **2003**, *278*, 11612−11622.
(33) Sgourakis, N. G.; Yan, Y.; McCallum, S. A.; Wang, C.; Garcia, A. E. The Alzheimer's peptides Aβ40 and 42 adopt distinct conformations in water: A combined MD/NMR Study. *J. Mol. Biol.* **2007**, *368*, 1448−1457.
(34) Vitalis, A.; Caflisch, A. Micelle-like architecture of the monomer ensemble of Alzheimer's amyloid-β peptide in aqueous solution and its implications for Aβ aggregation. *J. Mol. Biol.* **2010**, *403*, 148−165.
(35) Kim, S.; Takeda, T.; Klimov, D. K. Mapping conformational ensembles of Aβ oligomers in molecular dynamics simulations. *Biophys. J.* **2010**, *99*, 1949−1958.
(36) Masman, M. F.; Eisel, U. L. M.; Csizmadia, I. G.; Penke, B.; Enriz, R. D.; Marrink, S. J.; Luiten, P. G. M. *In silico* study of full-length amyloid β 1−42 tri- and penta-oligomers in solution. *J. Phys. Chem. B* **2009**, *113*, 11710−11719.
(37) Man, V. H.; Nguyen, P. H.; Derreumaux, P. High-Resolution structures of the amyloid-β 1−42 dimers from the comparison of four atomistic force fields. *J. Phys. Chem. B* **2017**, *121*, 5977−5987.
(38) Huang, T. H. J.; Yang, D.-S.; Plaskos, N. P.; Go, S.; Yip, C. M.; Fraser, P. E.; Chakrabartty, A. Structural studies of soluble oligomers of the Alzheimer β-amyloid peptide. *J. Mol. Biol.* **2000**, *297*, 73−87.
(39) Ahmed, M.; Davis, J.; Aucoin, D.; Sato, T.; Ahuja, S.; Aimoto, S.; Elliott, J. I.; Van Nostrand, W. E.; Smith, S. O. Structural conversion of neurotoxic amyloid-β 1−42 oligomers to fibrils. *Nat. Struct. Mol. Biol.* **2010**, *17*, 561−567.
(40) Ono, K.; Condron, M. M.; Teplow, D. B. Structure−neurotoxicity relationships of amyloid β-protein oligomers. *Proc. Natl. Acad. Sci. U. S. A.* **2009**, *106*, 14745−14750.
(41) Han, M.; Hansmann, U. H. E. Replica exchange molecular dynamics of the thermodynamics of fibril growth of Alzheimer's Aβ42 peptide. *J. Chem. Phys.* **2011**, *135*, 065101.
(42) Takeda, T.; Klimov, D. K. Replica exchange simulations of the thermodynamics of Aβ fibril growth. *Biophys. J.* **2009**, *96*, 442−452.
(43) Gurry, T.; Stultz, C. M. Mechanism of amyloid-β fibril elongation. *Biochemistry* **2014**, *53*, 6981−6991.
(44) Han, W.; Schulten, K. Fibril elongation by Aβ17−42: Kinetic network analysis of hybrid-resolution molecular dynamics simulations. *J. Am. Chem. Soc.* **2014**, *136*, 12450−12460.
(45) Schwierz, N.; Frost, C. V.; Geissler, P. L.; Zacharias, M. Dynamics of seeded Aβ40-fibril growth from atomistic molecular dynamics simulations: Kinetic trapping and reduced water mobility in the locking step. *J. Am. Chem. Soc.* **2016**, *138*, 527−539.
(46) Rodriguez, R. A.; Chen, L. Y.; Plascencia-Villa, G.; Perry, G. Elongation affinity, activation barrier, and stability of Aβ42 oligomers/fibrils in physiological saline. *Biochem. Biophys. Res. Commun.* **2017**, *487*, 444−449.
(47) Scheidt, H. A.; Morgado, I.; Rothemund, S.; Huster, D.; Fändrich, M. Solid-state NMR spectroscopic investigation of Aβ protofibrils: Implication of a β-sheet remodeling upon maturation into terminal amyloid fibrils. *Angew. Chem., Int. Ed.* **2011**, *50*, 2837−2840.
(48) Fawzi, N. L.; Ying, J.; Ghirlando, R.; Torchia, D. A.; Clore, G. M. Atomic-resolution dynamics on the surface of amyloid-β protofibrils probed by solution NMR. *Nature* **2011**, *480*, 268−272.
(49) Vitalis, A.; Pappu, R. V. Assessing the contribution of heterogeneous distributions of oligomers to aggregation mechanisms of polyglutamine peptides. *Biophys. Chem.* **2011**, *159*, 14−23.
(50) Hori, Y.; Hashimoto, T.; Wakutani, Y.; Urakami, K.; Nakashima, K.; Condron, M. M.; Tsubuki, S.; Saido, T. C.; Teplow, D. B.; Iwatsubo, T. The Tottori (D7N) and English (H6R) familial Alzheimer disease mutations accelerate Aβ fibril formation without increasing protofibril formation. *J. Biol. Chem.* **2007**, *282*, 4916−4923.
(51) Ono, K.; Condron, M. M.; Teplow, D. B. Effects of the English (H6R) and Tottori (D7N) familial Alzheimer disease mutations on amyloid β-protein assembly and toxicity. *J. Biol. Chem.* **2010**, *285*, 23186−23197.
(52) Jonsson, T.; Atwal, J. K.; Steinberg, S.; Snaedal, J.; Jonsson, P. V.; Bjornsson, S.; Stefansson, H.; Sulem, P.; Gudbjartsson, D.; Maloney, J.; Hoyte, K.; Gustafson, A.; Liu, Y.; Lu, Y.; Bhangale, T.; Graham, R. R.; Huttenlocher, J.; Bjornsdottir, G.; Andreassen, O. A.; Jonsson, E. G.; Palotie, A.; Behrens, T. W.; Magnusson, O. T.; Kong, A.; Thorsteinsdottir, U.; Watts, R. J.; Stefansson, K. A mutation in APP protects against Alzheimer/'s disease and age-related cognitive decline. *Nature* **2012**, *488*, 96−99.
(53) Snow, C. D.; Sorin, E. J.; Rhee, Y. M.; Pande, V. S. How well can simulation predict protein folding kinetics and thermodynamics? *Annu. Rev. Biophys. Biomol. Struct.* **2005**, *34*, 43−69.
(54) Bacci, M.; Vitalis, A.; Caflisch, A. A molecular simulation protocol to avoid sampling redundancy and discover new states. *Biochim. Biophys. Acta, Gen. Subj.* **2015**, *1850*, 889−902.
(55) Roux, B. The calculation of the potential of mean force using computer simulations. *Comput. Phys. Commun.* **1995**, *91*, 275−282.
(56) Han, W.; Schulten, K. Further optimization of a hybrid united-atom and coarse-grained force field for folding simulations: Improved backbone hydration and interactions between charged side chains. *J. Chem. Theory Comput.* **2012**, *8*, 4413−4424.
(57) Berezhkovskii, A.; Hummer, G.; Szabo, A. Reactive flux and folding pathways in network models of coarse-grained protein dynamics. *J. Chem. Phys.* **2009**, *130*, 205102.
(58) Lührs, T.; Ritter, C.; Adrian, M.; Riek-Loher, D.; Bohrmann, B.; Döbeli, H.; Schubert, D.; Riek, R. 3D structure of Alzheimer's amyloid-β (1−42) fibrils. *Proc. Natl. Acad. Sci. U. S. A.* **2005**, *102*, 17342−17347.
(59) Huang, J.; MacKerell, A. D. CHARMM36 all-atom additive protein force field: Validation based on comparison to NMR data. *J. Comput. Chem.* **2013**, *34*, 2135−2145.
(60) Pronk, S.; Páll, S.; Schulz, R.; Larsson, P.; Bjelkmar, P.; Apostolov, R.; Shirts, M. R.; Smith, J. C.; Kasson, P. M.; van der Spoel, D.; Hess, B.; Lindahl, E. GROMACS 4.5: A high-throughput and highly parallel open source molecular simulation toolkit. *Bioinformatics* **2013**, *29*, 845−854.
(61) Bussi, G.; Donadio, D.; Parrinello, M. Canonical sampling through velocity rescaling. *J. Chem. Phys.* **2007**, *126*, 014101.
(62) Blöchliger, N.; Vitalis, A.; Caflisch, A. A scalable algorithm to order and annotate continuous observations reveals the metastable states visited by dynamical systems. *Comput. Phys. Commun.* **2013**, *184*, 2446−2453.
(63) Wurth, C.; Guimard, N. K.; Hecht, M. H. Mutations that reduce aggregation of the Alzheimer's Aβ42 peptide: An unbiased search for the sequence determinants of Aβ amyloidogenesis. *J. Mol. Biol.* **2002**, *319*, 1279−1290.

DOI: 10.1021/acs.jctc.7b00662
J. Chem. Theory Comput. 2017, 13, 5117−5130

(64) Horn, A. H. C.; Sticht, H. Amyloid-β42 oligomer structures from fibrils: A systematic molecular dynamics study. *J. Phys. Chem. B* **2010**, *114*, 2219−2226.
(65) Goddard, T. D.; Huang, C. C.; Ferrin, T. E. Visualizing density maps with UCSF Chimera. *J. Struct. Biol.* **2007**, *157*, 281−287.
(66) Vitalis, A.; Caflisch, A. Efficient construction of mesostate networks from molecular dynamics trajectories. *J. Chem. Theory Comput.* **2012**, *8*, 1108−1120.
(67) Bowman, G. R.; Beauchamp, K. A.; Boxer, G.; Pande, V. S. Progress and challenges in the automated construction of Markov state models for full protein systems. *J. Chem. Phys.* **2009**, *131*, 124101.
(68) Stravalaci, M.; Beeg, M.; Salmona, M.; Gobbi, M. Use of surface plasmon resonance to study the elongation kinetics and the binding properties of the highly amyloidogenic Aβ1−42 peptide, synthesized by depsi-peptide technique. *Biosens. Bioelectron.* **2011**, *26*, 2772−2775.
(69) Kabsch, W.; Sander, C. Dictionary of protein secondary structure: Pattern recognition of hydrogen-bonded and geometrical features. *Biopolymers* **1983**, *22*, 2577−2637.
(70) Wright, P. E.; Dyson, H. J. Linking folding and binding. *Curr. Opin. Struct. Biol.* **2009**, *19*, 31−38.
(71) Zhang, S.; Iwata, K.; Lachenmann, M. J.; Peng, J. W.; Li, S.; Stimson, E. R.; Lu, Y. a.; Felix, A. M.; Maggio, J. E.; Lee, J. P. The Alzheimer's peptide Aβ adopts a collapsed coil structure in water. *J. Struct. Biol.* **2000**, *130*, 130−141.
(72) Chen, Y.-R.; Glabe, C. G. Distinct early folding and aggregation properties of Alzheimer amyloid-β peptides Aβ40 and Aβ42. *J. Biol. Chem.* **2006**, *281*, 24414−24422.
(73) Kim, Y. S.; Liu, L.; Axelsen, P. H.; Hochstrasser, R. M. 2D IR provides evidence for mobile water molecules in β-amyloid fibrils. *Proc. Natl. Acad. Sci. U. S. A.* **2009**, *106*, 17751−17756.
(74) Görbitz, C. H. The structure of nanotubes formed by dihpenylalanine, the core recognition motif of Alzheimer's β-amyloid peptide. *Chem. Commun.* **2006**, 2332−2334.
(75) Krone, M. G.; Hua, L.; Soto, P.; Zhou, R.; Berne, B. J.; Shea, J.-E. Role of water in mediating the assembly of Alzheimer amyloid-β Aβ16−22 protofilaments. *J. Am. Chem. Soc.* **2008**, *130*, 11066−11072.
(76) Reddy, G.; Straub, J. E.; Thirumalai, D. Dry amyloid fibril assembly in a yeast prion peptide is mediated by long-lived structures containing water wires. *Proc. Natl. Acad. Sci. U. S. A.* **2010**, *107*, 21459−21464.
(77) Wang, T.; Jo, H.; DeGrado, W. F.; Hong, M. Water distribution, dynamics, and interactions with Alzheimer's β-amyloid fibrils investigated by solid-state NMR. *J. Am. Chem. Soc.* **2017**, *139*, 6242−6252.
(78) Colvin, M. T.; Silvers, R.; Ni, Q. Z.; Can, T. V.; Sergeyev, I.; Rosay, M.; Donovan, K. J.; Michael, B.; Wall, J.; Linse, S.; Griffin, R. G. Atomic resolution structure of monomorphic Aβ42 amyloid fibrils. *J. Am. Chem. Soc.* **2016**, *138*, 9663−9674.
(79) Wälti, M. A.; Ravotti, F.; Arai, H.; Glabe, C. G.; Wall, J. S.; Böckmann, A.; Güntert, P.; Meier, B. H.; Riek, R. Atomic-resolution structure of a disease-relevant Aβ(1−42) amyloid fibril. *Proc. Natl. Acad. Sci. U. S. A.* **2016**, *113*, E4976−E4984.
(80) Maloney, J. A.; Bainbridge, T.; Gustafson, A.; Zhang, S.; Kyauk, R.; Steiner, P.; van der Brug, M.; Liu, Y.; Ernst, J. A.; Watts, R. J.; Atwal, J. K. Molecular mechanisms of Alzheimer's disease protection by the A673T allele of amyloid precursor protein. *J. Biol. Chem.* **2014**, *289*, 30990−31000.
(81) Di Fede, G.; Catania, M.; Morbin, M.; Rossi, G.; Suardi, S.; Mazzoleni, G.; Merlin, M.; Giovagnoli, A. R.; Prioni, S.; Erbetta, A.; Falcone, C.; Gobbi, M.; Colombo, L.; Bastone, A.; Beeg, M.; Manzoni, C.; Francescucci, B.; Spagnoli, A.; Cantù, L.; Del Favero, E.; Levy, E.; Salmona, M.; Tagliavini, F. A recessive mutation in the APP gene with dominant-negative effect on amyloidogenesis. *Science* **2009**, *323*, 1473−1477.
(82) Nasica-Labouze, J.; Nguyen, P. H.; Sterpone, F.; Berthoumieu, O.; Buchete, N.-V.; Coté, S.; De Simone, A.; Doig, A. J.; Faller, P.; Garcia, A.; Laio, A.; Li, M. S.; Melchionna, S.; Mousseau, N.; Mu, Y.; Paravastu, A.; Pasquali, S.; Rosenman, D. J.; Strodel, B.; Tarus, B.; Viles, J. H.; Zhang, T.; Wang, C.; Derreumaux, P. Amyloid β protein and Alzheimer's disease: When computer simulations complement experimental studies. *Chem. Rev.* **2015**, *115*, 3518−3563.
(83) Nguyen, P. H.; Sterpone, F.; Campanera, J. M.; Nasica-Labouze, J.; Derreumaux, P. Impact of the A2V mutation on the heterozygous and homozygous Aβ1−40 dimer structures from atomistic simulations. *ACS Chem. Neurosci.* **2016**, *7*, 823−832.
(84) Arimon, M.; Sanz, F.; Giralt, E.; Carulla, N. Template-assisted lateral growth of amyloid-β42 fibrils studied by differential labeling with gold nanoparticles. *Bioconjugate Chem.* **2012**, *23*, 27−32.
(85) Schmidt, M.; Sachse, C.; Richter, W.; Xu, C.; Fändrich, M.; Grigorieff, N. Comparison of Alzheimer Aβ(1−40) and Aβ(1−42) amyloid fibrils reveals similar protofilament structures. *Proc. Natl. Acad. Sci. U. S. A.* **2009**, *106*, 19813−19818.
(86) Schmidt, M.; Rohou, A.; Lasker, K.; Yadav, J. K.; Schiene-Fischer, C.; Fändrich, M.; Grigorieff, N. Peptide dimer structure in an Aβ(1−42) fibril visualized with cryo-EM. *Proc. Natl. Acad. Sci. U. S. A.* **2015**, *112*, 11858−11863.
(87) Paravastu, A. K.; Leapman, R. D.; Yau, W.-M.; Tycko, R. Molecular structural basis for polymorphism in Alzheimer's β-amyloid fibrils. *Proc. Natl. Acad. Sci. U. S. A.* **2008**, *105*, 18349−18354.
(88) Zhang, R.; Hu, X.; Khant, H.; Ludtke, S. J.; Chiu, W.; Schmid, M. F.; Frieden, C.; Lee, J.-M. Interprotofilament interactions between Alzheimer's Aβ1−42 peptides in amyloid fibrils revealed by cryoEM. *Proc. Natl. Acad. Sci. U. S. A.* **2009**, *106*, 4653−4658.
(89) Xiao, Y.; Ma, B.; McElheny, D.; Parthasarathy, S.; Long, F.; Hoshi, M.; Nussinov, R.; Ishii, Y. Aβ(1−42) fibril structure illuminates self-recognition and replication of amyloid in Alzheimer's disease. *Nat. Struct. Mol. Biol.* **2015**, *22*, 499−505.
(90) Wälti, M. A.; Orts, J.; Riek, R. Quenched hydrogen-deuterium exchange NMR of a disease-relevant Aβ(1−42) amyloid polymorph. *PLoS One* **2017**, *12*, e0172862.
(91) Cohen, S. I. A.; Linse, S.; Luheshi, L. M.; Hellstrand, E.; White, D. A.; Rajah, L.; Otzen, D. E.; Vendruscolo, M.; Dobson, C. M.; Knowles, T. P. J. Proliferation of amyloid-β42 aggregates occurs through a secondary nucleation mechanism. *Proc. Natl. Acad. Sci. U. S. A.* **2013**, *110*, 9758−9763.
(92) Jeong, J. S.; Ansaloni, A.; Mezzenga, R.; Lashuel, H. A.; Dietler, G. Novel mechanistic insight into the molecular basis of amyloid polymorphism and secondary nucleation during amyloid formation. *J. Mol. Biol.* **2013**, *425*, 1765−1781.
(93) Morris, A. M.; Watzky, M. A.; Agar, J. N.; Finke, R. G. Fitting neurological protein aggregation kinetic data via a 2-step, minimal/"Ockham's Razor" Model: the Finke−Watzky mechanism of nucleation followed by autocatalytic surface growth. *Biochemistry* **2008**, *47*, 2413−2427.
(94) Hasegawa, K.; Ono, K.; Yamada, M.; Naiki, H. Kinetic modeling and determination of reaction constants of Alzheimer's β-amyloid fibril extension and dissociation using surface plasmon resonance. *Biochemistry* **2002**, *41*, 13489−13498.
(95) Tseng, B. P.; Esler, W. P.; Clish, C. B.; Stimson, E. R.; Ghilardi, J. R.; Vinters, H. V.; Mantyh, P. W.; Lee, J. P.; Maggio, J. E. Deposition of monomeric, not oligomeric, Aβ mediates growth of Alzheimer's disease amyloid plaques in human brain preparations. *Biochemistry* **1999**, *38*, 10424−10431.

DOI: 10.1021/acs.jctc.7b00662
J. Chem. Theory Comput. 2017, 13, 5117−5130